CHAPTER 2

FABRICATION AND CHARACTERIZATION OF MoO_3 NANOSTRUCTURES

As seen in last chapter, MoO_3 is an interesting material for various applications. It has been shown that nanostructures exhibit properties distinct from bulk. To enhance its properties, many researches have been carried out on the fabrication of MoO_3 nanostructures using various techniques [43–48]. For instances, large–area MoO_3 nanowires were prepared on a silicon substrate by heating a Mo boat in vacuum [43, 44]. MoO_3 nanorods were synthesized by hydrothermal route or solution–based method [45, 46]. MoO_3 quasi–nanotubes have been prepared on a Ta substrate by infrared irradiation heating in high vacuum [47]. Also, MoO_3 nanospheres were prepared on a Si substrate by electrical heating of a Mo–coil [48]. Nanobelts of MoO_3 can be fabricated by many methods, such as solution–based methods [49, 50] and the high temperature method using metallic molybdenum [51, 52].

In this work, vapor transport method to fabricate MoO_3 single crystals was investigated. The method has ease of experimental set up and is a low–cost technique. With this method, mass production of MoO_3 whiskers was achieved. Due to the size

of crystals depending on the growth rate and time, the nanoscaled MoO_3 could be accessed by varying these two parameters. In addition, ion implantation technique as a new effective method was used to modify the surface of MoO_3 whiskers and also its electrical properties. Result from the surface modification showed that the ion implantation technique could lead to the formation of MoO_3 nanobelts and nanowires on the surface of MoO_3 whisker.

In this chapter, we discuss the fabrication of MoO_3 nanoplates by the vapor transport method and MoO_3 nanobelts and nanowires by the ion implantation technique. Characterizations of crystal morphologies, phase structure, and Raman scattering were carried out by scanning electron microscopy (SEM), transmission electron microscopy (TEM), and Raman spectroscopy, respectively. The effect of ion implantation on MoO_3 whisker properties will also be discussed.

2.1 Vapor transport method to fabricate MoO_3 nanoplates

Vapor transport method is commonly used to fabricate single crystals of various materials which have low boiling point. MoO_3 has sublimation point at 700°C. Single crystals of MoO_3 are easily fabricated using this method.

2.1.1 Fabrication

The fabrication of MoO_3 nanoplates was carried out in the following steps. MoO_3 powder (99.9% purity Fluka Chemical) was firstly compressed to form a pellet of 2 inches in diameter by hydrostatic force of 50 tons. The pellet was put inside a cylindrical alumina tubular furnace and heated up to 750^{o}C in normal atmosphere. Then, silicon (100) substrates were put vertically at different positions corresponding

to the temperatures of 680°C, 650°C, and 600°C, respectively, as shown in Fig. 2.1. After 10 minutes, the silicon substrates were moved out from the furnace. These substrates were covered with a transparent layer of MoO_3 product.

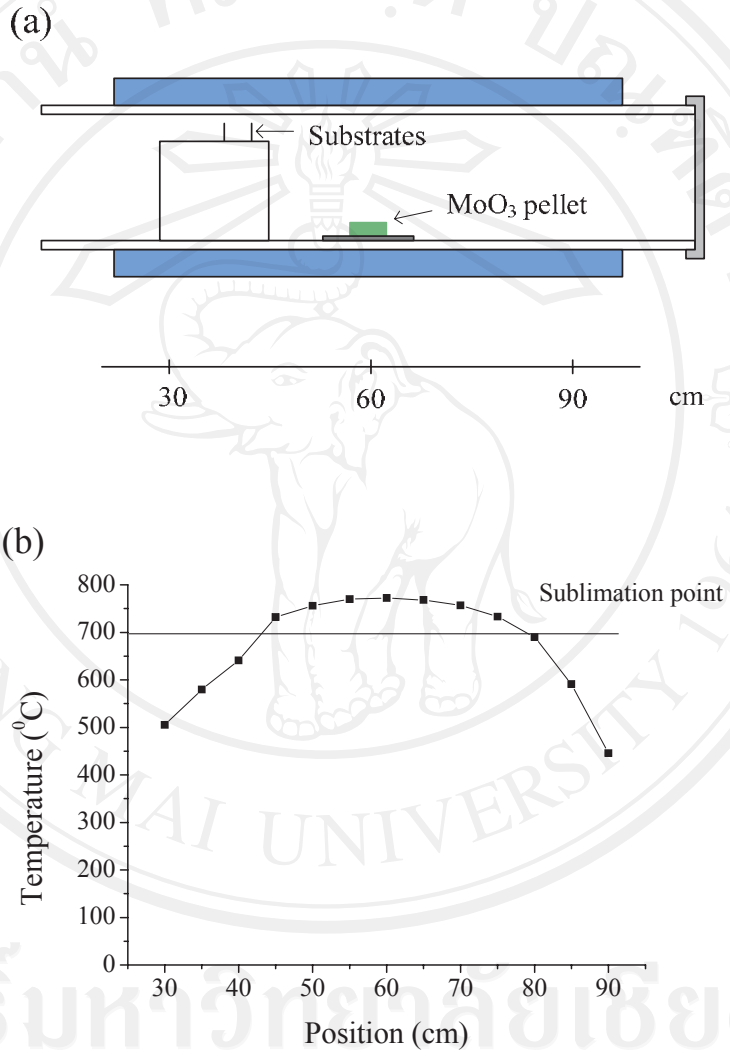

Figure 2.1 (a) Tubular furnace showing MoO_3 vapor source and Si substrate position. (b) Temperature inside the furnace as a function of position.

2.1.2 SEM and TEM Characterization

The morphology of the transparent layer was characterized by scanning electron microscopy (SEM; Jeol, JSM–6335F). It revealed that the transparent film was a plate–like structure as shown in Fig. 2.2. At 680°C, the MoO_3 nanoplates had clear facet and their edges were sharp as shown in Fig. 2.2a–b. At 600°C, the MoO_3 nanoplates were contaminated with aggregated particles and their edge was round as shown in Fig. 2.2c–d. The MoO_3 nanoplates, at 680°C, had a thickness of about 60–120 nm and a width of 1–4 μm.

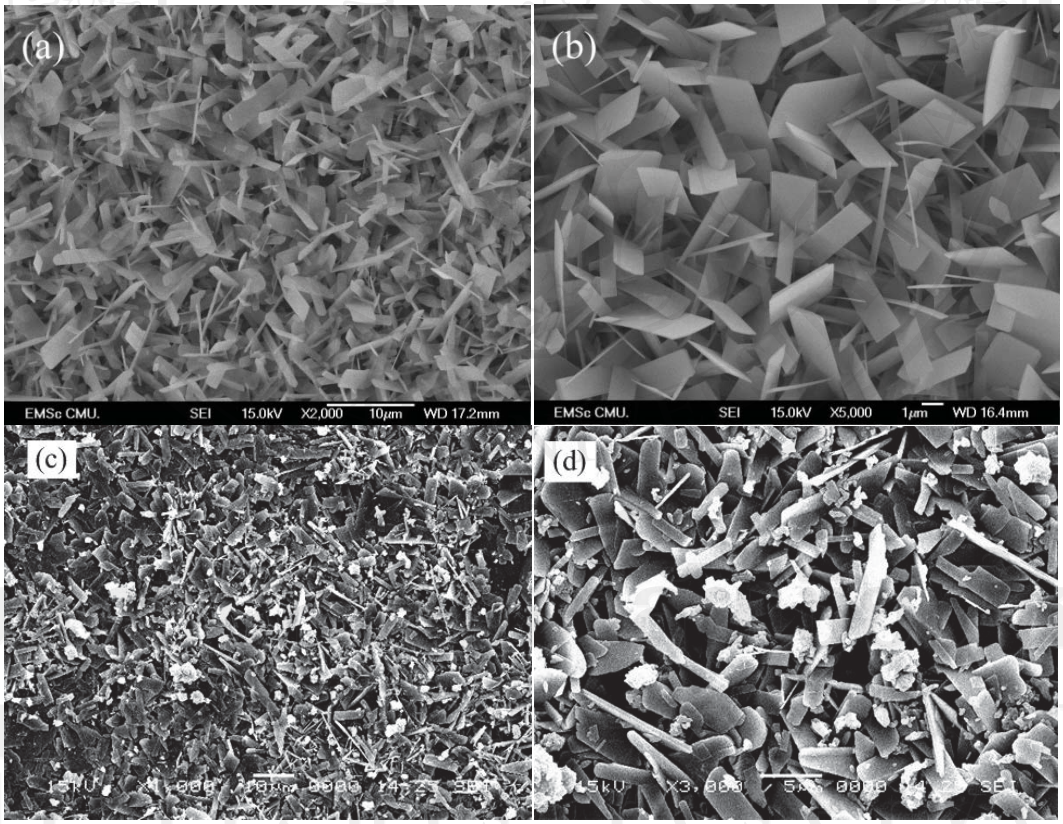

Figure 2.2 SEM images of MoO_3 nanoplates grown on silicon substrates: (a)–(b) at 680°C and (c)–(d) at 600°C.

MoO_3 started to sublime at temperatures higher than 700°C. The MoO_3 vapor generated from the MoO_3 pellet flowed along the tube to condense on the substrates at positions where the temperature was lower than 700°C. The formation of MoO_3 nanoplates could be due to the large difference of the close–packing rate between [010] and [100] directions. The growth mechanism will be explained in more detail in section 2.3. The unclear facet and aggregated particles on the MoO_3 product at 600°C could be induced by the large temperature gradient between the vapor source and the substrate. Moreover, the distance from the position at 700°C to the substrate was considered to affect the aggregation of MoO_3 particles on MoO_3 nanoplates. The longer distance, the more chance for MoO_3 vapor to aggregate before attaching on the substrate.

In this method, the size of MoO_3 crystals depended on the growth time. MoO_3 whiskers were grown by using longer time for Raman scattering study which will be mentioned in the following section.

2.1.3 Raman scattering

Raman scattering of the MoO_3 whiskers was studied using the 514.5 nm Ar^+ laser with a backscattering optical configuration. The orientation of the whiskers and the laser polarization were taken into account for analysis. Fig. 2.3 shows the Raman spectra of the MoO_3 whiskers in the frequency range of 50–1100 cm^{-1}. All the Raman peaks observed were in good agreement with the literature [53]. The intensity of the Raman peaks varies based on the crystal orientation and polarization of the laser

source. Beattie and Gilson [54] have applied group frequency to the vibration spectra of metal oxide. Three main regions appear for the MoO_3 vibration at 1000–600, 400–200, and below 200 cm^{-1} which correspond respectively to the stretching, deformation, and lattice modes. The Raman peaks observed in this research will be discussed together with data for a single crystal MoO_3 reported by Py and Maschke [53].

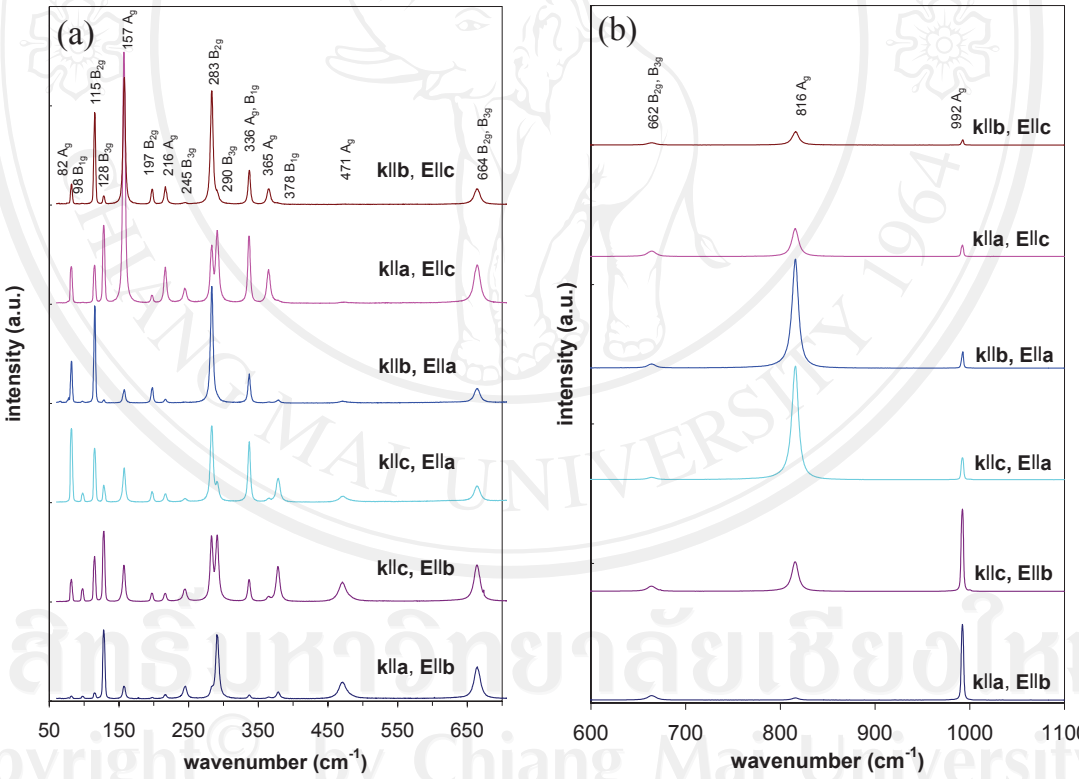

Figure 2.3 Raman spectra of MoO_3 whiskers taken from six cases of crystal orientation and polarization, (a) in the range of 50 – 700 cm^{-1} and (b) in the range of 650–1100 cm^{-1} with the intensity eight times stronger than that in (a).

The Raman peaks at 992 and 816 cm^{-1} are the A_g mode. This corresponds to the ν_{as} Mo=O1 stretching in which the bonding aligns along the **b** axis direction and the ν_s Mo–O3–Mo stretching in which the bonding aligns along the **a** axis direction, respectively. This results in a drastically change of intensity when polarization occurs in these directions. The peak at 664 cm^{-1} is the B_{2g} and B_{3g} modes which corresponds to the ν_{as} Mo–O2 stretching in which the three bondings lie in the **bc** plane. Although the MoO_3 spectrum might not be obviously noticeable but, from Table 2.1, its intensity should be higher in the case of the wave propagates parallel with the **a** and with the **b** axes. The peak at 471 cm^{-1} is the A_g mode which corresponds to the ν_{as} Mo–O2 stretching and bending. This peak appeared only in the case of using polarization aligned along the **b** axis direction. This resulted in the Mo–O2 bonding to be stretched by 2.33 Å along the **b** axis direction. The peak at 378 cm^{-1} is the B_{1g} mode, corresponding to the δ O2–Mo–O2 scissor.

The Raman tensors corresponding to A_g, B_{1g}, B_{2g}, and B_{3g} are

$$\begin{pmatrix} \alpha'_{xx} & 0 & 0 \\ 0 & \alpha'_{yy} & 0 \\ 0 & 0 & \alpha'_{zz} \end{pmatrix}, \begin{pmatrix} 0 & \alpha'_{xy} & 0 \\ \alpha'_{xy} & 0 & 0 \\ 0 & 0 & 0 \end{pmatrix}, \begin{pmatrix} 0 & 0 & \alpha'_{xz} \\ 0 & 0 & 0 \\ \alpha'_{xz} & 0 & 0 \end{pmatrix}, \text{ and } \begin{pmatrix} 0 & 0 & 0 \\ 0 & 0 & \alpha'_{yz} \\ 0 & \alpha'_{yz} & 0 \end{pmatrix},$$

respectively. These Raman tensors lead to the selection rules for the six cases of our experiment as given in Table 2.1.

From Table 2.1, its Raman intensity should be the maximum in the case of the wave propagates parallel with the **c** axis. All experimental results described above were in good agreement with the selection rules (see Fig. 2.3a for the cases of $k \parallel \mathbf{c}$ & $E \parallel \mathbf{a}$ and $k \parallel \mathbf{c}$ & $E \parallel \mathbf{b}$).

The peak at 365 cm^{-1} is the A_g mode and therefore corresponds to the δ O2–Mo–O2 scissor. Its Raman intensity is maximum in the case of polarization along the **c** axis direction, due to the variation of the angle between the two 1.95 Å Mo–O2 bondings lying in the **b–c** plane and corresponds to the selection rule. The peaks at 283 and 290 cm^{-1} are the B_{2g} and B_{3g} modes. This corresponds to the δ O1=Mo=O1 wagging. The B_{2g} mode intensity should be higher in the case of the propagation parallel with the **b** axis than that of other cases whereas the B_{3g} mode intensity should be higher in the case of the propagation parallel with the **a** axis.

The peak at 245 cm^{-1} is the B_{3g} mode, corresponding to the τ O1=Mo=O1 twist. These results were in agreement with the selection rules in this mode. The peak at 216 cm^{-1} is the A_g mode, corresponding to the rotational rigid MoO_4 chain mode, R_c. This peak appeared only in the case when polarization was along with the **c** axis direction. The peak at 157 cm^{-1} is the A_g mode. This corresponds to the δ $(O_2Mo_2)_n$ polyhedron along with the chain axis. Its intensity increased strongly when polarizing along the **c** axis direction. The peaks at 82, 98, 115, and 128 cm^{-1} are the A_g, B_{1g}, B_{2g}, and B_{3g} modes, respectively, corresponding to the translational rigid MoO_4 chain mode. The intensity of the A_g peak was at the maximum when polarizing along the **a** axis. According to the selection rules, the B_{1g}, B_{2g}, and B_{3g} intensities were at the maximum in the case of the propagation along with **c**, **b**, and **a** axis directions, respectively.

Table 2.1 Raman selection rules for backscattering corresponding to all possible cases [30].

Cases	Scattering configuration	Allowed modes	Tensor components
$k \parallel \mathbf{a}, E \parallel \mathbf{b}$	$x(yy)\bar{x}$	A_g	α'_{yy}
	$x(yz)\bar{x}$	B_{3g}	α'_{yz}
$k \parallel \mathbf{a}, E \parallel \mathbf{c}$	$x(zz)\bar{x}$	A_g	α'_{zz}
	$x(zy)\bar{x}$	B_{3g}	α'_{yz}
$k \parallel \mathbf{b}, E \parallel \mathbf{a}$	$y(xx)\bar{y}$	A_g	α'_{xx}
	$y(xz)\bar{y}$	B_{2g}	α'_{xz}
$k \parallel \mathbf{b}, E \parallel \mathbf{c}$	$y(zz)\bar{y}$	A_g	α'_{zz}
	$y(zx)\bar{y}$	B_{2g}	α'_{xz}
$k \parallel \mathbf{c}, E \parallel \mathbf{a}$	$z(xx)\bar{z}$	A_g	α'_{xx}
	$z(xy)\bar{z}$	B_{1g}	α'_{xy}
$k \parallel \mathbf{c}, E \parallel \mathbf{b}$	$z(yy)\bar{z}$	A_g	α'_{yy}
	$z(yx)\bar{z}$	B_{1g}	α'_{xy}

2.2 Ion implantation technique

Ion implantation is a new technique to fabricate nanostructures of materials [55]. During the modification of a MoO_3 whisker surface by the ion implantation technique, the electrical property of MoO_3 was also changed. It was found that this technique had the ability to generate nanostructures on the MoO_3 whisker surface.

2.2.1 Fabrication of MoO_3 nanobelts and nanowires

The synthesis was based on nitrogen or carbon ion implantation into 1–2 mm width MoO_3 whiskers which were grown by using the vapor transport method. In general, the ion implantation process is used to implant the required atoms or ions inside matter. However, in this work the heat generated inside the matter was also important. A varian ion implanter model 200–DF5 was employed in this experiment. Two sets of MoO_3 whiskers were attached to two aluminum plates (0.8 mm x 53 mm x 80 mm) by silver paint. The first set was implanted with 60 keV nitrogen ions (N^+) for 40 minutes with a dose of $1x10^{16}$ atom/cm^2 under pressure of $2x10^{-5}$ mbar. The second set was implanted with 60 keV carbon ions (C^+) for 30 minutes with the same dose under the same pressure. In the process the aluminum plate was placed vertically in a holder which contacted cooling water system (~16°C) in the vacuum chamber. The ion beam was controlled to be rectangularly scanning over the aluminum plate. After implantation, the whiskers changed their physical features from colorless to soft purple.

2.2.2 SEM and TEM characterization

A field emission scanning electron microscopy [(FE–SEM) JSM–6700F] was used to observe the morphology of the implanted whisker surface. Belt–like nanostructures were found on some parts of the N^+ implanted whiskers whereas wire–like nanostructures were found on some parts of the C^+ implanted whiskers. MoO_3 nanobelts were also characterized by a transmission electron microscope [(TEM) JEM–300F].

A lot of nanobelts were found on the whisker surfaces near the silver paint area, as depicted in Fig. 2.4a and b. Few and shorter nanobelts were found on other areas and no nanostructure occurred in the middle of some whiskers due to high temperature. The nanobelts had grown and laid randomly on the whisker surfaces near the silver paint area, as shown in Fig. 2.4a. A high–magnification image of the nanobelts, as seen in Fig. 2.4b, showed that the nanobelts had the width in the range of 20–60 nm and the length in the range of 300–800 nm. The unclear SEM image of the nanobelts was due to the low electrical conductivity of the nanobelts. A large area of nanowires was shown in Fig. 2.4c. Most of nanowires had grown upward and aligned randomly. A closer view of the nanowires, Fig. 2.4d, showed that size of nanowires was about 50–200 nm in diameter and 300–1000 nm in length. The clear SEM image of the nanowires suggested that the conductivity of nanowires was higher than that of nanobelts.

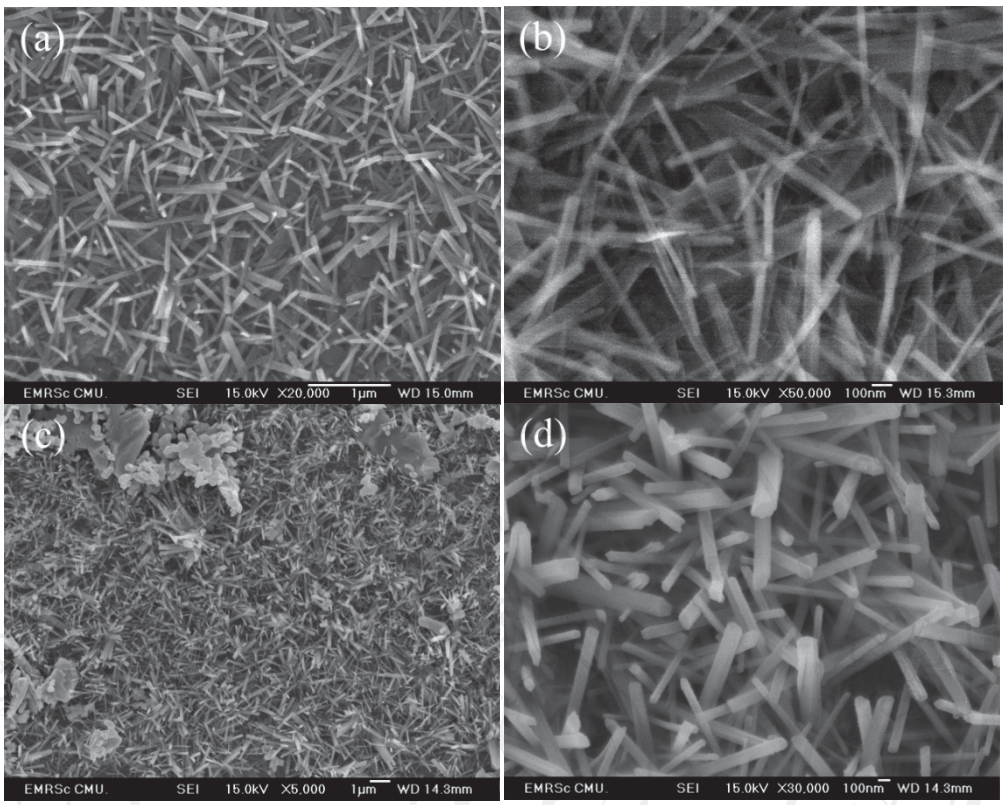

Figure 2.4 SEM images of the surface (a) and (b) on the N^+ implanted whiskers (c) and (d) on the C^+ implanted whiskers.

Further characterization of the nanobelts was done by TEM operating at 200 kV. A typical TEM image and selected area electron diffraction (SAED) pattern corresponding to the TEM image of the nanobelts are shown in Fig. 2.5a. They revealed that the nanobelt was single crystalline with some polycrystalline impurity indicated by a ring around the central spot of the SAED pattern. The presence of polycrystalline phase was probably induced by the penetration of the nitrogen ions during the implantation. The nanobelts have grown in the longitudinal direction lying along the [001] direction of the orthorhombic MoO_3, similar to previously reported

[49–52]. In addition, the higher magnification TEM image revealed that the surface of the nanobelts grown under ion bombardment process was rough, as seen in Fig. 2.5b.

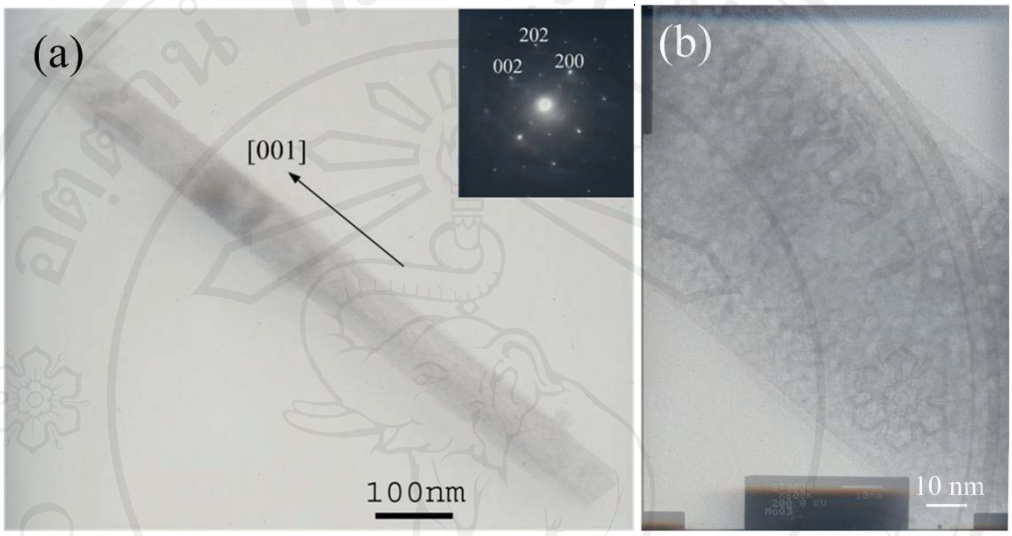

Figure 2.5 (a) Representative TEM image and (b) higher magnification TEM micrograph of nanobelts. The inset in (a) shows the corresponding SAD pattern taken with the incident beam in the <010> direction.

2.2.3 Effect of ion implantation on Raman scattering

The ion implantation was performed to the MoO_3 whisker specimen under 60 keV of nitrogen ion energy with a dose of $5x10^{16}$ atom/cm^2 in system pressure of $2x10^{-5}$ mbar. In addition, the ion implanter was also different. The nitrogen ions were extracted from the ion source and moved forward directly to the target without using the mass analyzer, so that both N^+ and N_2^+ were in the beam. The nitrogen ions were then implanted into the whiskers. After the implantation process, it could be observed

that the implanted whiskers changed from transparent to semi–transparent. Basically, the penetrability of heavy ion is worse than that light ion. Therefore, N_2^+ could penetrate in the whisker shallower than N^+. Hence, the nitrogen depth distribution in the whisker was different from previous subsection.

Fig. 2.6a shows the Raman spectra of the implanted MoO_3 whiskers in comparison to that of the unimplanted MoO_3 whiskers. No extra peaks appeared on the entire Raman spectrum of the N^+ implanted whiskers. The intensity of these peaks decreased approximately one order of magnitude with respect to that of the unimplanted whiskers. However, in the case of the wave propagation parallel to the **a** axis and the polarization parallel to the **c** axis, the inset in Fig. 2.6a, the I_{290}/I_{283} ratio of the implanted whiskers was approximately 2.5 times higher than that of the unimplanted whiskers. This was determined by using Gaussian curve fitting. The graph in Fig. 2.6b shows the relative suppressions of the implanted–Raman peaks of the symmetry modes with respect to the A_g symmetry mode at 816 cm^{-1}. From this graph, it can be seen that most of the A_g, B_{1g}, and B_{2g} modes were suppressed with the same ratio whereas all of the B_{3g} modes (see the peaks 4, 8, 10, and 15 in Fig. 2.6b) were suppressed with a ratio lower than that of the other modes. Therefore, the B_{3g} modes had a higher ratio of I/I_{816} with respect to the unimplanted ratio, which was derived from the case of the wave propagation parallel to the **a** axis; $k \parallel \mathbf{a}$. No other propagation directions have such an observable difference.

The results of Raman intensity decreasing resemble that of the reported H^+ ion implantation on a pellet of MoO_3 with a dose lower than $4x10^{16}$ ions/cm^2 [56]. This could be explained based on the electronic screening of phonons in the metallic state

that the electron transfers from hydrogen to Mo. Therefore, a similar situation could be applied to our results. M. Dieterle et al. [57] have studied the Raman spectrum of various stoichiometry of MoO_{3-x}. They have found that the ratio of I_{283}/I_{290} decreased linearly as a function of the stoichiometry x, *i.e.* oxygen vacancy concentration. On the other hand, the distortion due to oxygen vacancy existing in the crystal structure caused the Raman intensity of the B_{3g} mode at 290 cm^{-1} to increase with respect to the B_{2g} mode at 283 cm^{-1}. The comparison between the ratio of I/I_{816} from a single crystal and from polycrystal or film by summing all cases of orientation can be seen in Fig. 2.6b. This graph suggests that after the implantation, the ratio of I_{283}/I_{290} decreased which was in agreement with what has been observed by M. Dieterle et al. However, it was worth to summarize that not only the B_{3g} mode at 290 cm^{-1} but all of the B_{3g} modes increased with respect to other modes. This is due to the distortion of the crystal structure from the ion implantation except for the case of the wave propagation parallel with the **a** axis; $k \parallel \mathbf{a}$.

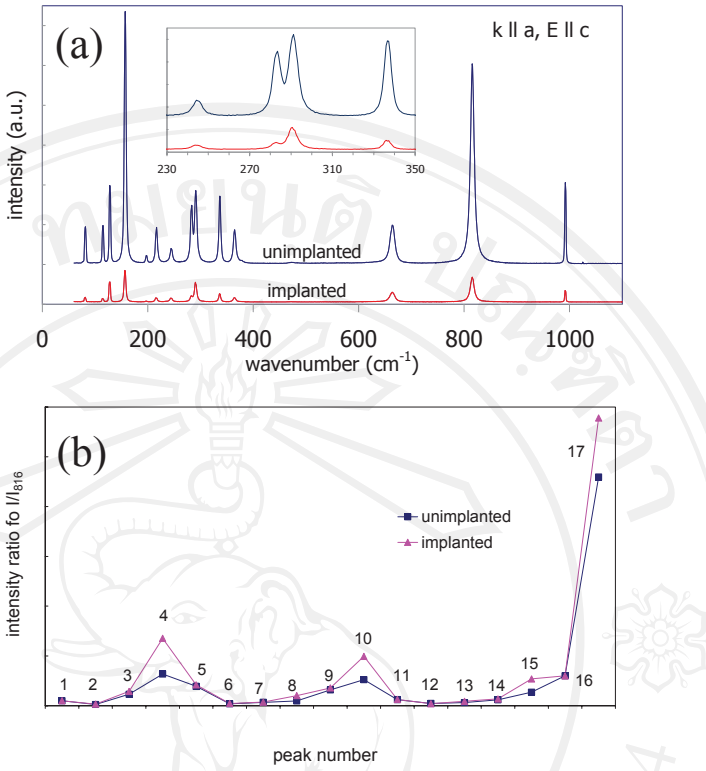

Figure 2.6 Raman spectra of implanted and unimplanted MoO_3 whiskers in the case of the wave propagation parallel to the **a** axis and polarization parallel to the **c** axis (a) in the range of 60–1100 cm^{-1} and the inset of (a) expand the range of 230–350 cm^{-1} to show implantation effect on the intensity ratio of I_{283}/I_{290}. (b) The intensity ratio I/I_{816} of the implanted whiskers in comparison to the unimplanted whiskers, where the peaks 1–17 are Raman peaks at 82, 98, 115,..., and 992 cm^{-1}, respectively where each peak is the summation of the ratio from all six cases.

2.2.4 Effect of ion implantation on electrical properties

The electrical conductivity of the whiskers was measured by using the HP E3633A DC power supply and the HP 34970A multimeter at temperatures ranging

from 25–200ºC. A Hall measurement was also used to explore the electrical concentration of the implanted whiskers in this research. From the Raman analysis, it was found that the nitrogen ion implantation caused oxygen vacancies and other defects. In theory, the defects of a semi–conducting crystal could enhance the electrical conductivity. In this research, the electrical conductivity (σ) as a function of temperature for the implanted MoO_3 whiskers specimens was determined, as shown in Fig. 2.7. This could be represented by the expression below [58],

$$\sigma = A\exp(-E_a / kT) \qquad (2.1)$$

where A is Arrhenius constants, E_a is the activation energy for the conduction processes, k is the Boltzmann constant and T is the specimen temperature in Kelvin.

From the curve fitting of the data collected from the experiments, the expression above could be written as:

$$\sigma = 3.58x10^{-1}\exp(\frac{-0.041eV}{kT})\Omega^{-1}cm^{-1} \qquad (2.2)$$

The activation energy of implanted whiskers was about 0.041 eV. The conductivity was enhanced to about 0.074 $\Omega^{-1}cm^{-1}$ at a room temperature. This is approximately seven orders of magnitude greater than that of the results from Pandit et al. [59], From the Hall measurement, the implanted whiskers exhibited as an n–type semiconductor and their electron concentration was about $7x10^{16}$ cm^{-3}. As reported in the literature [59, 60], MoO_3 exhibits electrical conductivity differently in two regions of temperature. Pandit et al. reported that the higher temperature region was above 380ºC for a single crystal. The activation energy of this region was about 1.75 eV

which can be referred to as the intrinsic conduction. For the lower temperature region, the activation energy was about 0.05 eV which was in good agreement with our results. This low activation energy can be categorized as the extrinsic conduction due to impurity, point defects or interstitials, which could not be removed easily [61] and often present in the forbidden gap of the crystal. They also pointed out that at a low temperature, MoO_3 was n–type semiconductor whose band gap energy was approximately 3.5 eV whereas at high temperature it became p–type. Traditionally, if any oxygen atom in the MoO_3 crystal structure was replaced by the nitrogen atom which has less number of valence electrons, then the MoO_3 crystal structure should exhibit as p–type. This was not fit into our case. From the Raman analysis, it is confirmed that this is due to the nitrogen ions, which was regarded as impurity, inserted into the layer of the MoO_3 structure. In other words, the implantation of nitrogen ions may increase the electrical conductivity by forming a shallow donor which can be referred to as the n–type conductivity.

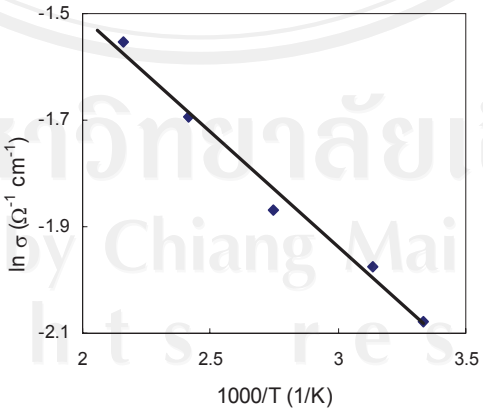

Figure 2.7 Electrical conductivity as a function of temperature for the implanted MoO_3 whiskers.

2.3 Growth mechanism of MoO_3 nanostructures

In the VS mechanism, the size of MoO_3 crystals is proportional to time and growth rate which depend on evaporation rate and system pressure. Theoretically, the formation of plate–like or belt–like nanostructures can be explained by the kinetics of crystal growth via the 2D nucleation probability [62] which is expressed as

$$P_N = B\exp(-\frac{\pi\sigma^2}{k^2T^2\ln(\alpha)}) \qquad (2.3)$$

where P_N is a nucleation probability, B is a constant, σ is the surface energy of the solid whisker, k is the Boltzmann constant, T is the absolute temperature, and α is the supersaturation ratio defined as $\alpha = p/p_0$, in which p is vapor pressure and p_0 is the equilibrium vapor pressure corresponding to temperature T. A higher temperature and larger supersaturation ratio lead to plate–like structure. In comparison, lower temperature and smaller supersaturation ratio promote the growth of wire/belt–like structure.

In vapor transport method, the 2D nucleation probability was easily used to explain the formation of the MoO_3 nanoplates. The preparation of the MoO_3 nanoplastes was performed under conditions of atmosphere pressure and high evaporation rate of MoO_3 vapor. These conditions led to a large supersaturation ratio, resulting the formation of MoO_3 single crystals in plate–like structure.

In the ion implantation process, each nitrogen ion carried energy of 60 keV to hit the whiskers and aluminum plate. By using the transport of ion in matter (TRIM) program [63] to calculate the energy of the nitrogen ions loss in MoO_3 matter, about

65 percent of the energy was used to ionize atoms in the target and then changed into heat energy when the atoms returned to original status, while the remaining energy was used to generate phonons. However, it was hard to estimate the temperature in MoO_3 whiskers. Therefore, temperature in aluminum plate was estimated. The temperature in the MoO_3 whiskers could be approximated as higher than the temperature in the aluminum plate because the MoO_3 whiskers have a lower heat capacity and were bombarded with the same amount of nitrogen ions per unit area as the aluminum plate. Under unrigorous calculation based on the bombardment of the 60 keV nitrogen ions about $2x10^{12}$ ion/cm^2–sec onto the aluminum plate (53mm x 80 mm x 0.8 mm), the temperature in the aluminum plates was expected to rise to about 500ºC at the end of the implantation process with a temperature rate of 0.21ºC/sec. Certainly, the actual temperature of the aluminum plates should be lower than this temperature because some of the heat should transfer to the holder and the water cooling system. Therefore, the temperature of the MoO_3 whiskers could be higher than 500ºC. As shown in phase diagram of MoO_3, Fig. 2.8, solid-vapor transition could occur at below 700°C in vacuum ($2x10^{-5}$ mbar). Moreover, the sublimation point of MoO_3 is about 700ºC [64] at atmospheric pressure. This suggested that MoO_3 could sublime at lower temperature in our case. Hence, the actual temperature of the MoO_3 whiskers was high enough to evaporate them. In this ion implantation process, nitrogen ions penetrated into the MoO_3 whiskers to the depth of about 240 nm and its maximum concentration occurred at the depth of about 110 nm, both calculated by the TRIM program. Hence the hottest point was 110 nm inside the whiskers. Vapor was generated inside the whiskers with low evaporation rate and then flowed out to condense at lower temperature near the whisker surfaces, as depicted in Fig. 2.9.

Since there was a large pressure difference between the vapor source inside the whiskers and the whisker surfaces, some of the vapor could flow quickly into the vacuum when it was generated. Hence, MoO_3 crystals gradually formed with VS mechanism to be MoO_3 nanostructures. Since the MoO_3 crystals have an orthorhombic structure with the lattice parameter: **a** = 3.96 Å, **b** = 13.86 Å, and **c** = 3.70 Å, it should be grown preferentially in the **c** direction due to lowest surface energy of (001) plane and belt–like structure should be formed due to large differences in close–packing rate among (100) and (010) plane. As mentioned, at the regions near the silver paint area, the denser and longer nanobelts were observed because these regions were better attached to the aluminum plate and had lower temperature than the middle part of the whiskers. The nanobelts could not be grown at the middle of some whiskers as the temperature of those parts was too high, leading to the re–evaporation effect.

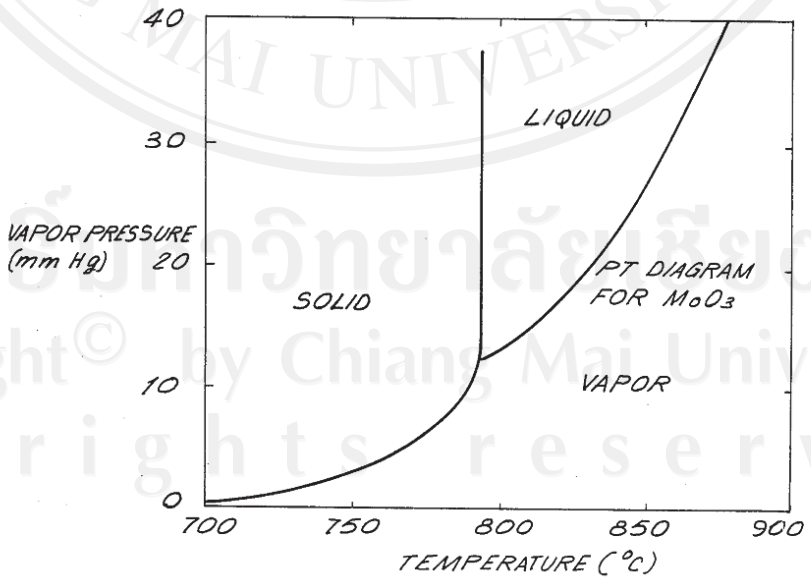

Figure 2.8 Phase diagram of MoO_3 [65]

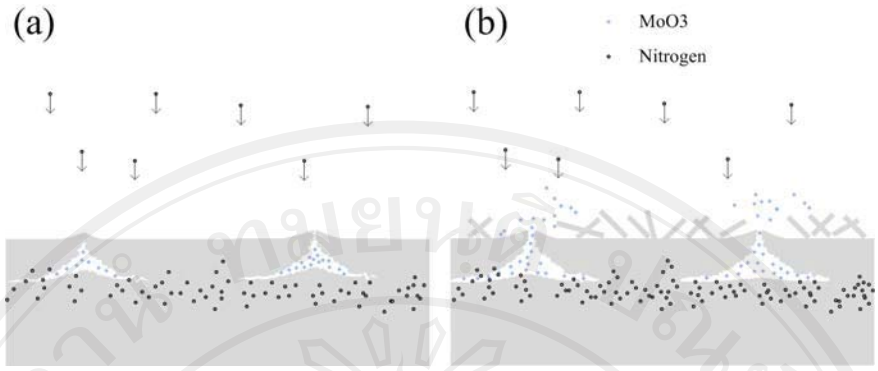

Figure 2.9 The purposed growth process of MoO_3 nanobelts: (a) starting crack due to high vapor pressure and (b) formation of the MoO_3 vapor on the surface.